






Thermal resistance at a twist boundary and a semicoherent heterointerface

Ramya Gurunathan ¹, Riley Hanus ^{2,†}, Samuel Graham ², Anupam Garg ³, and G. Jeffrey Snyder ^{1,*}

¹Department of Materials Science and Engineering, Northwestern University, Evanston, Illinois 60208, USA

²George W. Woodruff School of Mechanical Engineering, Georgia Institute of Technology, Atlanta, Georgia 30332, USA

³Department of Physics and Astronomy, Northwestern University, Evanston, Illinois 60208, USA



(Received 5 January 2021; revised 5 March 2021; accepted 19 March 2021; published 8 April 2021; corrected 14 April 2021)

Traditional models of interfacial phonon scattering, including the acoustic mismatch model and diffuse mismatch model, take into account the bulk properties of the material surrounding the interface, but not the atomic structure and properties of the interface itself. Here, we derive a theoretical formalism for the phonon scattering at a dislocation grid, or two interpenetrating orthogonal arrays of dislocations, as this is the most stable structure of both the symmetric twist boundary and semicoherent heterointerface. With this approach, we are able to separately examine the contribution to thermal resistance due to the step-function change in acoustic properties and due to interfacial dislocation strain fields, which induces diffractive scattering. Both low-angle Si-Si twist boundaries and the Si-Ge heterointerfaces are considered here and compared to previous experimental and simulation results. This work indicates that scattering from misfit dislocation strain fields doubles the thermal boundary resistance of Si-Ge heterointerfaces compared to scattering due to acoustic mismatch alone. Scattering from grain boundary dislocation strain fields is predicted to dominate the thermal boundary resistance of Si-Si twist boundaries. This physical treatment can guide the thermal design of devices by quantifying the relative importance of interfacial strain fields, which can be engineered via fabrication and processing methods, versus acoustic mismatch, which is fixed for a given interface. Additionally, this approach captures experimental and simulation trends such as the dependence of thermal boundary resistance on the grain boundary angle and interfacial strain energy.

DOI: [10.1103/PhysRevB.103.144302](https://doi.org/10.1103/PhysRevB.103.144302)

I. INTRODUCTION

Given the ubiquity of interfaces and grain boundaries in engineering materials, estimating their influence on thermal transport is essential to the design of devices like integrated circuits and thermoelectrics, particularly in the age of nanostructuring [1–3]. The current standard models of thermal boundary resistance (or Kapitza resistance, R_K), which are the acoustic mismatch model (AMM) and diffuse mismatch model (DMM), only consider the properties of the media surrounding the interface, but ignore the interfacial defect structure [4–10]. Even the recently introduced strain mismatch model (SMM) [7], an *ab initio* framework applied to compute the phonon coupling to the long-range dilatation at a Si-Ge heterointerface, neglects the periodic, local strain fields induced by the interfacial defects [7]. Therefore, trends in thermal resistance with modifications to the local interface structure cannot be easily discerned. Molecular dynamics (MD) simulations, however, have revealed an interplay between R_K and the interface structure and geometry [5,8,11].

While computational techniques such as MD have been useful in probing the atomic-scale structure at interfaces [5,8,11,12], the continuum-theory-based model presented

here provides valuable insights into phonon scattering sources at the nanometer to micron length scale from strain fields at the interface. Therefore, our theoretical approach to thermal boundary resistance enables the multiscale modeling of thermal materials in an integrated computational materials engineering (ICME) framework [1,13,14]. Atomic simulation-based techniques require separate evaluations for every interface structure, whereas this model provides a critical analytical link between thermal boundary resistance, material properties, and grain boundary configurations. As in most work on this problem to date, we treat the scattering in terms of a fixed perturbation. The dynamical degrees of freedom within the interface are ignored, and inelastic scattering in which an interfacial phonon is absorbed or emitted is thus not accounted for. Treating inelastic boundary scattering remains an open problem, although early molecular and lattice dynamics simulations suggest that coupling to localized interfacial modes can influence optical phonon transport at an interface [15,16].

Recent experimental work on grain boundaries and heterointerfaces suggests that insights into the role of interfacial dislocation structure on thermal resistance will be highly impactful [17]. For example, the periodic dislocation structure present at low-angle grain boundaries has been associated with significant thermal conductivity reductions and improvements in the thermoelectric performance of well-studied materials such as bismuth antimony telluride [18,19]. While

*jeff.snyder@northwestern.edu

†hanusriley@gmail.com

several experimental investigations exist for the ensemble average interface scattering in a polycrystal, individual grain boundary types are difficult to study. However, recent R_K measurements using the 3ω method on fabricated twist bicrystals of Si [20] and Al_2O_3 [21] point to evidence of dislocation strain scattering as a dominant mechanism. For example, the thermal boundary resistance R_K of these twist boundaries is shown to depend on the grain boundary angle or, equivalently, the dislocation spacing, in addition to the interfacial strain energy. In both the Si and Al_2O_3 twist boundaries, transmission electron microscopy (TEM) imaging has been used to verify the presence of dislocation arrays at the interface [20,21]. Additionally, heterointerfaces are often intentionally created in thermal materials through a variety of nanostructuring techniques including heterostructures, thin-film superlattices, and nanoprecipitate boundaries [1,22]. Thus far, it has been difficult to experimentally determine the effect of misfit dislocations—which can in some cases be controlled through annealing and interlayer thickness—on thermal resistance. Our model, which quantifies the relative importance of interfacial dislocation strain versus acoustic mismatch, can help answer questions about the degree of registry at an interface required to suppress phonon transmission.

In our previous work, a strain scattering theory was used to model the one-dimensional (1D) array of edge dislocations at a symmetric tilt grain boundary, which predicted a frequency (ω)-dependent relaxation time, in contrast to standard models [23]. The frequency dependence was essential to capture the anomalous low-temperature thermal conductivity trend of $\kappa \propto T^2$ in polycrystalline materials [23–26]. Here, we extend this framework to interfacial structures in which two interpenetrating arrays of dislocations form a cross grid. The grid geometry allows us to describe the anharmonic strain scattering of other low-energy grain boundaries common to engineering materials. These include twist boundaries and semicoherent heterointerfaces, which can be decomposed into a grid of screw-type and misfit edge-type dislocations, respectively (see pp. 688–700 of Ref. [27]) (Fig. 1). The dislocation strain scattering mainly affects mid-frequency phonons with wavelengths on the order of the dislocation spacing. High-frequency phonons would couple strongly to the atomic inhomogeneities at the dislocation core. We arrive at the interfacial strain scattering potential by superposing single-dislocation-line scattering potentials. This strategy is only applicable for grain boundary angles of less than 15° in most materials, because the overlapping dislocation core regions dominate at higher grain boundary angles [28].

There are two main contributions to the scattering potential in this model. The first is the localized strain fields from the dislocation cross grid, and the second is the mismatch in acoustic properties between sides 1 and 2 of the interface. To illustrate these two contributions, we show in Fig. 2 the analytically calculated dilatational component ϵ_{yy} of the strain tensor for a simplified heterointerface in which there is lattice mismatch in one direction only and thus only one array of misfit dislocations. As is evident, the dilatation behaves asymptotically like a step function, but the large nonzero value of ϵ_{yy} as $|x| \rightarrow \infty$ is spurious, since it is being defined with reference to a fictitious average lattice. The actual reference lattice differs on the two sides of the interface.

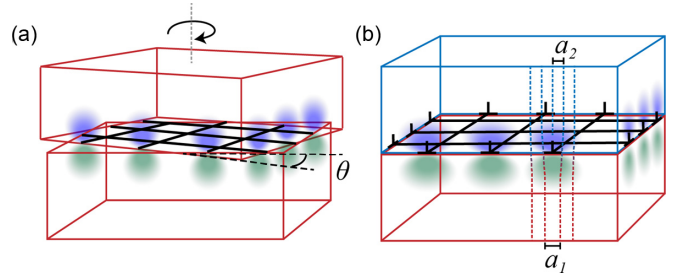


FIG. 1. Interfaces described by a grid of linear defects. (a) Schematic of a twist boundary with misorientation angle θ . The black lines indicate screw dislocations and the blue and green shading indicates shear strain. (b) A semicoherent heterointerface between two materials with lattice constants a_1 and a_2 . The black lines indicate edge dislocations and the blue and green shading indicates hydrostatic strain.

The true or *physical strain*, ϵ_{eff} , must be defined with respect to the true reference lattice, and is obtained by subtracting off the dilatation step function. This strain is much more localized to the vicinity of the interface. As highlighted in Fig. 2(b), the physical strain scatters via the lattice anharmonicity, while the step-function change in lattice parameter and the harmonic properties of the lattice are treated as an acoustic impedance mismatch. One benefit of our approach is the ease of separating the relative scattering contributions of the acoustic mismatch and dislocation strain in each grain boundary type.

In relation to the components of the scattering potential, a unique aspect of our work is the ability to recognize the very different character of phonon scattering with nonzero and zero \mathbf{Q}_{\parallel} , the (lattice) momentum transfer parallel to the interface. Scattering with $\mathbf{Q}_{\parallel} \neq 0$ necessarily arises from the dislocation structure within the interface, and therefore emerges from anharmonic interactions with the resulting strain. By contrast, scattering with $\mathbf{Q}_{\parallel} = 0$ washes out the atomistic variations in the interfacial structure, and is dominated by the abrupt change in the *harmonic* lattice properties in the bulk materials on the two sides of the interface, or acoustic mismatch, analogous to the refraction of light. In the twist boundary case, the acoustic mismatch stems from a rotation of the elastic tensor at the boundary. In the case of a semicoherent heterointerface, it stems from entering a new elastic medium, with an attendant change in the entire elastic tensor.

This separation of the two types of scattering manifests itself in our analysis as follows. In Ref. [23], it was shown that the periodic array of dislocations behaves like a diffraction grating, whereby the momentum transfer parallel to the dislocation lines vanishes and that in the direction of periodicity is quantized in units of $2\pi/D$ with D being the periodicity or the distance between the dislocation lines. An identical restriction must now apply to each of the two dislocation arrays in the cross grid. Because these arrays are mutually orthogonal, the constraints on momentum transfer imposed by each one separately cannot be satisfied simultaneously, and there is no interference between the scattering from one and the other. The arrays act as essentially independent scatterers. The exception is when the momentum transfer is zero along both the dislocation line directions, i.e., when $\mathbf{Q}_{\parallel} = 0$. Such scattering events correspond to either specular reflection or forward

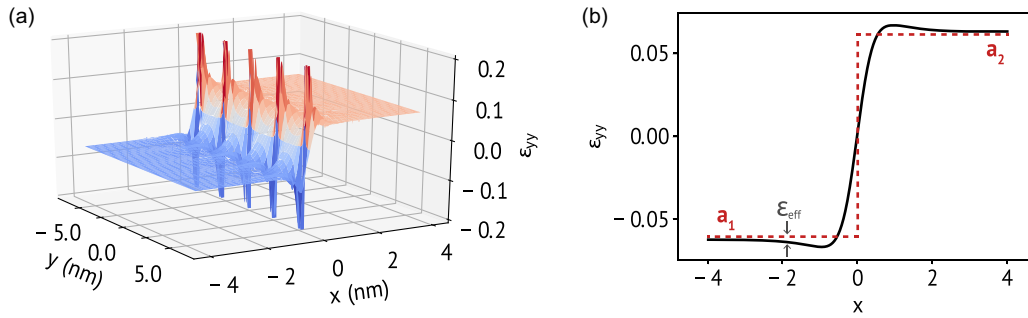


FIG. 2. Scattering at a semicoherent heterointerface stems from the periodic strain fields at a misfit dislocation array as well as the step-function change in acoustic impedance. (a) Analytic solution for the dilatational strain field component ϵ_{yy} from an infinite array of misfit dislocations periodically spaced along the y axis (see pp. 695–697 of Ref. [27]). (b) Cross section of three-dimensional (3D) dilatational strain field, showing an underlying step function (dotted red line). This is indicating a change in lattice parameter (a) from material 1 to 2, rather than long-range strain. We subtract off the step function in strain, and instead treat this effect with an acoustic mismatch scattering term. This leaves the physical strain (ϵ_{eff}), which we treat with an anharmonic strain scattering potential.

scattering, which are precisely what the acoustic mismatch addresses. For these events, therefore, we apply a different scattering potential for acoustic mismatch by modeling it as a step-function change in harmonic phonon properties, specifically the acoustic velocity. While our treatment handles this mismatch scattering within quantum perturbation theory, the magnitude of the transmissivity agrees well with the classical acoustic mismatch model [29]. We acknowledge that the limits of perturbation-type methods and their application to phonon-grain boundary or phonon-interface interactions is an open debate. We hope this work demonstrates the utility of this approach.

The plan of the paper is as follows. In Sec. II we present the interface scattering theoretical framework and apply it to a grid of linear defects. We discuss the scattering kinematics, and present the scattering potentials describing both the dislocation strain and the acoustic mismatch. These potentials are used to calculate a phonon scattering rate τ^{-1} using Fermi's golden rule. This rate is then used to compute a phonon transmissivity and, in turn, the thermal boundary resistance (R_K). Next, we apply the framework to a twist boundary (Si-Si in particular) in Sec. III, and to a semicoherent heterointerface (Si-Ge in particular) in Sec. IV. For both cases, we compare the R_K results to experimental measurements and various simulation techniques. The predicted R_K values agree with previous computational results from molecular dynamics [8,11,30], lattice dynamics [15], and atomistic Green's function analysis [31], and capture experimentally observed R_K trends with grain boundary angle and interfacial energy. Our model also shows that dislocation strain is the majority contribution to R_K for the Si-Si twist boundary and half of the contribution to R_K for the Si-Ge heterointerface. Our conclusions are summarized in Sec. V. The details of the scattering rate calculation, its relation to the Landauer formalism of phonon transmissivity, and the strain fields of the two types of interface, are given in the Appendixes.

II. THEORETICAL FRAMEWORK

The scattering theory employed here uses Fermi's golden rule to relate a real-space scattering potential $V(\mathbf{r})$ to a phonon scattering rate $\Gamma(\mathbf{q})$, and follows the notation and methodol-

ogy of Hanus *et al.* [23]. The scattering probability $W_{\mathbf{q},\mathbf{q}'}$ from phonon mode \mathbf{q} to \mathbf{q}' is defined in terms of the perturbation matrix element $\langle \mathbf{q} | H' | \mathbf{q}' \rangle$ for the corresponding process while enforcing conservation of energy [23]:

$$W_{\mathbf{q},\mathbf{q}'} = \frac{2\pi}{\hbar} |\langle \mathbf{q} | H' | \mathbf{q}' \rangle|^2 \delta(E_{\mathbf{q}'} - E_{\mathbf{q}}). \quad (1)$$

Restrictions on allowed \mathbf{q} -to- \mathbf{q}' transitions are discussed in Sec. II A. The scattering rate or inverse relaxation time $\tau(\mathbf{q})^{-1}$ of a phonon mode \mathbf{q} can then be calculated as the integral of $W_{\mathbf{q},\mathbf{q}'}$ over all possible final phonon states \mathbf{q}' , weighted to suppress nonresistive forward-scattering processes. Considering a grain of dimensions¹ $L_x \times L_y \times L_z$, the scattering rate expression simplifies to

$$\begin{aligned} \tau(\mathbf{q})^{-1} &= \Gamma(\mathbf{q}) \\ &= \frac{2\pi}{\hbar L_x L_y L_z} \iiint \frac{d^3 \mathbf{q}'}{(2\pi)^3} |M(\mathbf{Q})|^2 (1 - \hat{\mathbf{q}} \cdot \hat{\mathbf{q}}') \delta(E_{\mathbf{q}'} - E_{\mathbf{q}}). \end{aligned} \quad (2)$$

In the Born approximation, the scattering matrix element $M(\mathbf{Q}) \equiv L_x L_y L_z \langle \mathbf{q} | H' | \mathbf{q}' \rangle$ depends on the scattering vector $\mathbf{Q} = \mathbf{q}' - \mathbf{q}$. The scattering matrix element can, in turn, be written in terms of a real-space scattering potential $V(\mathbf{r})$ as

$$M(\mathbf{Q}) = \iiint d^3 r V(\mathbf{r}) e^{i\mathbf{Q} \cdot \mathbf{r}}. \quad (3)$$

We take this grain to contain a single low-angle grain boundary or semicoherent interface planning the entire yz plane. As explained in Sec. I, depending on whether \mathbf{Q}_{\parallel} is nonzero or not, we will model $V(\mathbf{r})$ as the perturbation due to either the strain fields of the periodic dislocation array, or the acoustic mismatch produced by the step-function change in elastic properties (see Sec. II B).

From the τ derived in Eq. (2), we can then compute the phonon transmissivity α_{12} from side 1 to side 2 of the interface. This is done by relating the Landauer and interfacial

¹While the final solution is only dependent on intensive properties, and is therefore independent of the volume or shape of the body, a brick-shaped grain is assumed to simplify the calculation.

scattering approaches for computing interfacial thermal resistance [32]. The transmissivity α_{12} can be expressed in terms of the relaxation time τ , side 1 group velocity v_{g1} , and the distance between interfaces or grain size L_x as

$$\alpha_{12} = \frac{v_{g1}\tau}{\frac{3}{4}L_x + v_{g1}\tau}. \quad (4)$$

In Appendix B, we provide a derivation of this equation along with an analysis showing that our perturbation treatment for acoustic mismatch transmissivity agrees within 5% of the classical acoustic mismatch model (given in Ref. [4] and here in Eq. (B12)), even when the relative change in phonon velocity across the interface $\Delta v/v$ is as much as 50%.

The end product of our calculation is the thermal boundary conductance (inversely, the thermal boundary or Kapitza resistance, R_K). This is computed from the perspective of either side of the interface using the transmissivity as an input [29]. We integrate up to the maximum phonon frequency ω_m , the product of the side 1 spectral heat capacity $C_1(\omega)$ and group velocity $v_{g1}(\omega)$, as well as the transmissivity at the interface from side 1 to side 2, $\alpha_{12}(\omega)$, and the reverse direction, $\alpha_{21}(\omega)$ [29,32–34]:

$$1/R_K = \frac{1}{4} \int_0^{\omega_m} C_1(\omega) v_{g1}(\omega) \left(\frac{\alpha_{12}(\omega)}{1 - \bar{\alpha}(\omega)} \right) d\omega. \quad (5)$$

Here, $\bar{\alpha}(\omega) = (\alpha_{12}(\omega) + \alpha_{21}(\omega))/2$. This treatment of the transmissivity factor arises by considering the local equilibrium temperature for incident and outgoing phonons [29,33,34]. It resolves the Kapitza paradox where, if the factor in the parentheses is replaced by $\alpha_{12}(\omega)$, a system with a transmissivity of $\alpha_{12} = 1$ would have a nonzero resistance, which is unphysical. The modification of the parenthetical factor is important for interfaces with high transmissivities such as twist boundaries. The transmissivity and phonon velocities are often temperature independent, and so the temperature dependence of R_K enters solely through the spectral heat capacity [29].

To summarize, a real-space scattering potential $V(\mathbf{r})$ is defined from the defect perturbation and used to compute the perturbation matrix element $M(\mathbf{Q})$. The scattering rate τ^{-1} is then calculated using Fermi's golden rule. From the relaxation time τ , additional transport properties including the phonon transmissivity α and thermal boundary resistance R_K are computed.

We would like to note that our implementation of the model is not polarization specific. Therefore, we do not evaluate the complex mode conversions at the boundary of two elastic solids. In this aspect, our implementation is similar to that of analytic models such as the AMM and DMM [29]. The phonons in this model are described by a Born–von Kármán dispersion parametrized using the mode-averaged speeds of sound listed in Table VI.

The following sections provide additional details about the scattering kinematics of this problem, as well as the strain and acoustic mismatch scattering potentials present at grain boundaries and heterointerfaces.

A. Scattering kinematics

As mentioned, several grain boundary geometries are composed of two dislocation arrays forming a cross grid. In the twist boundary case, for example, two sets of screw dislocation arrays each shear the crystal to induce a full rotation (see Fig. 3) [35]. We adopt the configuration in Fig. 4(a), with the x direction normal to the interface, and two orthogonal dislocation arrays with dislocation lines in the y and z directions. We will refer to the first dislocation array as the YZ array, where the first label (y) indicates the direction of periodicity, and the second label (z) indicates the direction of the dislocation line [see Fig. 4(a)]. The second array is likewise called the ZY array. The scattering potential of the cross grid is given by summing over the single-dislocation-line scattering potentials (V_1 ; see Sec. II B 1) for each array and then combining both,

$$V(\mathbf{r}) = \sum_{n=-\infty}^{\infty} V_1(x, y - nD) + \sum_{m=-\infty}^{\infty} V_1(x, z - mD). \quad (6)$$

Here, n and m can assume all integer values from $-\infty$ to $+\infty$. The infinite sums over n and m can be obtained analytically for both the twist and heterointerface cases [27,36] and are shown in Appendix C.

For simplicity, we focus on the contribution of the YZ array in the following steps, but analogous expressions can be written for the ZY array, by instead enforcing periodicity in the z direction. The Fourier transform of this sum of dislocation scattering potentials is

$$\begin{aligned} \tilde{V}_{YZ}(Q_x, Q_y) &= \iint dx dy \sum_{n=-\infty}^{\infty} V_1(x, y - nD) e^{-i(Q_x x + Q_y y)} \\ &= \sum_{n=-\infty}^{\infty} e^{-iQ_y nD} \tilde{V}_1(Q_x, Q_y). \end{aligned} \quad (7)$$

We show the Fourier transform of the scattering potential (\tilde{V}_1) as a function of only Q_x and Q_y , because the scattering vector along the line of the dislocation (Q_z) is necessarily zero [37]. By the Poisson summation formula [see Eq. (A3)], this simplifies to

$$\begin{aligned} \tilde{V}_{YZ} &= \frac{2\pi}{D} \sum_{n'=-\infty}^{\infty} \delta(Q_y - Q_{n'}) \tilde{V}_1(Q_x, Q_{n'}), \quad \text{with} \\ &\times \left(Q_{n'} = \frac{2\pi n'}{D} \right). \end{aligned} \quad (8)$$

As noted by Hanus *et al.* [23], this equation shows that phonon diffraction peak conditions will occur whenever the magnitude of the scattering wave-vector component Q_y equals $2\pi n'/D$ in an infinite interface [37–39]. Equation (3) can then be used to calculate the perturbation matrix element, resulting in

$$M(\mathbf{Q}) = 2\pi \delta(Q_z) \tilde{V}_{YZ}(Q_x, Q_y) + 2\pi \delta(Q_y) \tilde{V}_{ZY}(Q_x, Q_z). \quad (9)$$

As enforced by the δ functions, the scattering due to the YZ array is only nonzero when $Q_z = 0$, while scattering due to the ZY array is only nonzero when $Q_y = 0$. As a result, except when $Q_y = Q_z = 0$, the two dislocation arrays

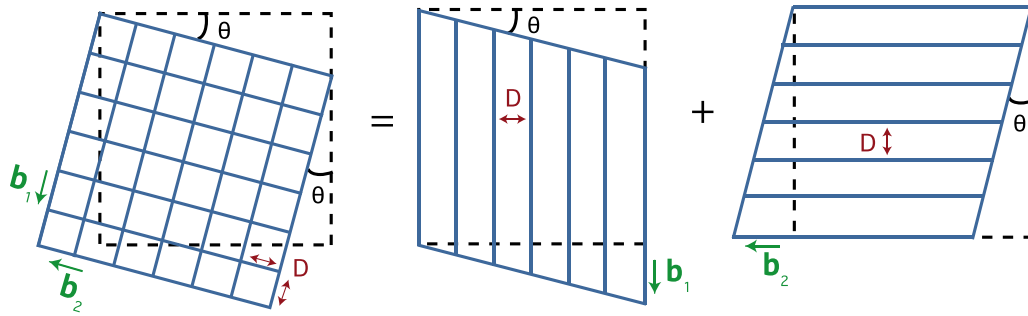


FIG. 3. Schematic of two orthogonal screw dislocation arrays, with Burgers vectors \mathbf{b}_1 and \mathbf{b}_2 , respectively, producing a twist misorientation (θ) at an interface.

scatter independently [see Fig. 4(b)]. The van der Merwe method for calculating interfacial strain energies [36] makes a similar assertion, namely, that the energy of both arrays can be reasonably computed separately and then superposed. Specifically analyzing the $Q_y = Q_z = 0$ condition reveals that this scenario must represent either a nonresistive forward-scattering case or a mirrorlike reflection. The underlying, periodic structure of the interface is washed out at this long-wavelength limit. We treat this scattering separately in terms of the acoustic impedance mismatch (see Sec. II B 2). The total scattering rate Γ is then the sum of the rates due to the YZ and ZY array, as well as that due to acoustic mismatch (AM) [see Eq. (15)]:

$$\Gamma_{\text{tot}} = \Gamma_{\text{YZ}} + \Gamma_{\text{ZY}} + \Gamma_{\text{AM}}. \quad (10)$$

Here, Γ_{YZ} entails only $|\tilde{V}_{\text{YZ}}|^2$, Γ_{ZY} entails only $|\tilde{V}_{\text{ZY}}|^2$, and Γ_{AM} entails only $|\tilde{V}_{\text{AM}}|^2$ [see Eqs. (14) and (15)]. To avoid misunderstanding, we note that the resemblance of Eq. (10) to Matthiessen's rule is superficial. The Γ_{AM} component does not represent a separate scattering channel but rather a completely independent kind of interface scattering, which is, in addition, activated at a different frequency regime.

Specifically, the scattering rate Γ_{YZ} due to periodic strain from the YZ array is

$$\Gamma_{\text{YZ}}(\mathbf{q}) = \frac{n_b}{\hbar^2 D^2} \sum_{n'=-\infty}^{\infty} \iiint d^3 \mathbf{q}' \delta(Q_z) \delta(\omega_{\mathbf{q}} - \omega_{\mathbf{q}'}) \times |\tilde{V}_{\text{YZ}}(Q_x, Q_y)|^2 (1 - \hat{\mathbf{q}} \cdot \hat{\mathbf{q}}'). \quad (11)$$

Here, n_b is equal to $1/L_x$ and represents the linear density of boundaries in the material. The result for Γ_{ZY} is similar.

With the scattering constraints imposed by defect geometry handled, the final step is to define scattering potentials from the interface properties. In the next section, we derive an anharmonic scattering potential from the interfacial dislocation strain fields, as well as a scattering potential from acoustic mismatch, which couples to phonons via harmonic elastic constants.

B. Scattering potentials

1. Dislocation strain

The real-space strain scattering potential or lattice energy perturbation is directly related to the induced internal strain $\epsilon(\mathbf{r})$ at the interface via an anharmonic coefficient, which in this case is the Grüneisen parameter [$\gamma = (1/\omega)d\omega/d\epsilon$]. A single Grüneisen parameter approximation is made wherein γ is frequency and mode independent, so that the change in phonon frequency due to internal strain is $\omega\gamma\epsilon(\mathbf{r})$. This approximation may lead to an underestimation of the phonon scattering, but trends with misorientation and comparisons of grain boundary geometry should still hold [23,40]. The scattering potential due to the strain from a single interfacial dislocation, $\epsilon_1(\mathbf{r})$, is

$$V_1(\mathbf{r}) = \hbar\omega\gamma\epsilon_1(\mathbf{r}). \quad (12)$$

We use the dislocation strain fields from continuum elasticity theory as given, for example, by Hirth and Lothe (see

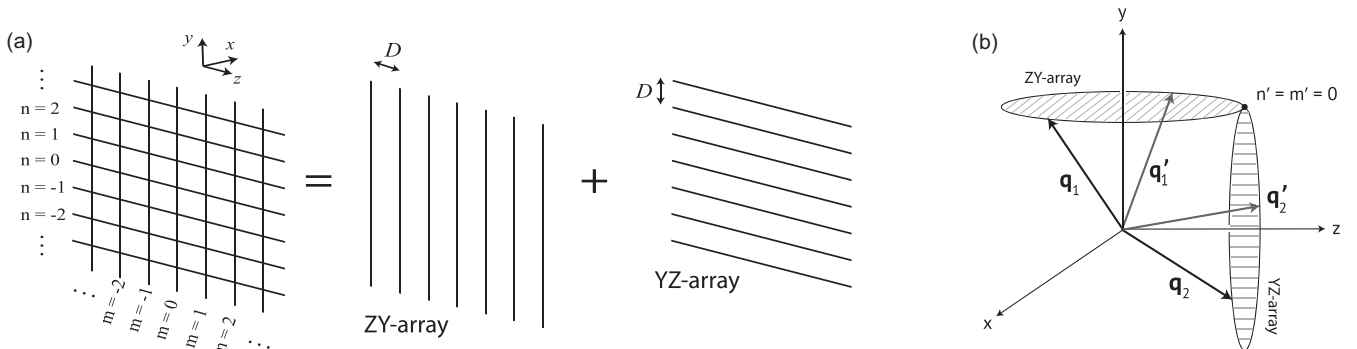


FIG. 4. (a) Diagram of orthogonal YZ and ZY arrays in dislocation cross grid. In this case, equal D spacing is assumed for both. (b) Phase-space diagram portraying the independent scattering of the YZ and ZY dislocation array, which overlap only at the $\mathbf{Q}_{\parallel} = 0$ ($n' = m' = 0$) condition.

pp. 60, 76 of Ref. [41]). As discussed in the previous section, the sum over single-line-dislocation potentials is facilitated in Fourier space, so all we require is the Fourier-transformed strain fields for a single screw and misfit-edge dislocation (similar to methods proposed in Refs. [7,23]). These are provided in Secs. III A and IV A, respectively.

2. Acoustic mismatch

In the case of the semicoherent heterointerface, the acoustic impedance mismatch stems from the change in material, and resulting change in elastic tensor, across the interface. In the twist boundary case, the long-range rotational deformation induces acoustic mismatch through the anisotropy of the acoustic properties. The rotation at a twist boundary is described by a single misorientation angle θ (see Fig. 3), which in the Read-Shockley model relates to the magnitude of the Burgers vector (b) and the dislocation spacing (D) as $2 \tan(\theta/2) = b/D$ (see p. 688 of Ref. [27]). For a fixed phonon angle of incidence, the crystal rotation can be interpreted as a change in the acoustic impedance stemming from the rotation of the stiffness tensor. For both grain boundaries and heterointerfaces, an acoustic mismatch scattering potential can be determined, which is grounded in the same physics as the classical AMM [8].

We define the scattering potential as the change in energy of a phonon as it traverses an interface, which can be expressed in terms of the change in phonon phase velocity Δv_p and incident phonon wave-vector magnitude q ,

$$V_{\text{AM}}(\mathbf{r}) = \hbar \Delta \omega(\mathbf{r}) = \hbar \Delta v_p(\mathbf{r})q. \quad (13)$$

The spatial dependence of $\Delta v_p(\mathbf{r})$ is taken as $\Delta v \Theta(x)$, where $\Delta v = v_2 - v_1$ is the magnitude of the phonon velocity change from side 1 to side 2, and $\Theta(x)$ is the Heaviside step function. Since its Fourier transform is $\tilde{\Theta}(Q_x) = i/(Q_x)$,

$$\tilde{V}_{\text{AM}} = \hbar \Delta v q \tilde{\Theta}(Q_x) = \hbar \Delta v \frac{iq}{Q_x}. \quad (14)$$

The magnitude of the velocity change Δv depends on the phonon angle of incidence and the degree of misorientation at a grain boundary or homointerface, and, at a heterointerface, the additional change in elastic tensor. We use the solver provided by Jaeken *et al.* [42] to solve the Christoffel equation (which is essentially the classical limit of the lattice dynamical matrix diagonalization) and compute the direction-dependent group and phase velocities of the acoustic phonons directly from the stiffness matrix (Appendix E). From these direction-dependent velocities, we can calculate Δv for an incoming phonon and capture the acoustic mismatch due to any grain boundary misorientation or change in elastic coefficients, regardless of crystal symmetry. Our implementation lies within the continuum, long-wavelength limit, and so V_{AM} computed using the magnitude of either the group or the phase velocity yields the same result given that the perturbation is set only by the change in phonon frequency. The acoustic mismatch constitutes planar defect scattering, and as mentioned previously, will produce a specular reflection. Since forward scattering does not contribute to the scattering rate, Q_x in Eq. (14) will simplify to $2q_x$.

Our treatment agrees with the conceptual conclusions from the work of Brown [43], which suggests that rotations of the crystal scatter phonons via harmonic elastic constants while strain scatters via third-order elastic constants [43]. In Appendix B, Fig. 10(b), we compare this perturbation theory treatment of acoustic mismatch scattering to the classical AMM result and show that they agree within 5% for velocity mismatches typical of solid-solid interfaces. To avoid issues with the change of reference frame, especially when handling the scattering effects due to the long-range deformation, we define the wave-vector directions and the lattice perturbations with reference to a virtual average lattice and ensure that the scattering potential is symmetric at the boundary [44].

Finally, the square of the Fourier space scattering potential must be taken in the calculation of the matrix element (M). In the work of Brown [43], it was shown that symmetry constraints in the cubic crystal enforce that strain and rotation contribute independently to the scattering potential. We reach the same conclusion in our work by noting the distinct scattering physics of strain (diffractive scattering) and rotation (specular reflection). As a result, there are no nonzero cross terms when we take the square and the full, squared scattering potential can be written as

$$|\tilde{V}(\mathbf{Q})|^2 = |\hbar \omega \gamma \tilde{\epsilon}(\mathbf{Q})|^2 + |\hbar \Delta v \tilde{\Theta}(x)q|^2. \quad (15)$$

Figure 5 shows the phonon scattering rate plotted versus the incident angle of the incoming phonon for a twist boundary. It provides a visual representation of the rotation versus strain scattering effects. At high frequency, the diffraction effects stemming from the periodic dislocation array are visible as patterns in the directional plot of scattering rate, whereas at low frequency, there are more isolated and broad scattering ‘‘hot spots’’ corresponding to ranges in the phonon angle of incidence which undergo large scattering due to an acoustic impedance mismatch [10].

III. TWIST BOUNDARY SCATTERING

In this section, we aim to construct a model that explicitly considers the strain effects of the interfacial screw dislocations present at low-angle twist boundaries, while also treating the rotational deformation.

A. Twist boundary strain fields

The strain scattering potential of a screw dislocation grid can be described using Eqs. (6) and (12). We will maintain the geometry of the previous section with the x direction normal to the interface and dislocation arrays with sense vectors oriented along the y and z directions. The strain state of a twist boundary is pure shear, such that all components ϵ_{ii} are zero. Only two independent components of the strain tensor are nonzero for each dislocation array. These are given in real space in Appendix C. Table I lists the strain component Fourier transforms for a constituent screw dislocation in either the YZ or ZY array.

It is a textbook result that while a single array of screw dislocations produces a long-range shear stress, the two periodic screw dislocation arrays in a twist boundary cancel each other’s long-range stress field (see pp. 699–700 of Ref. [27]).

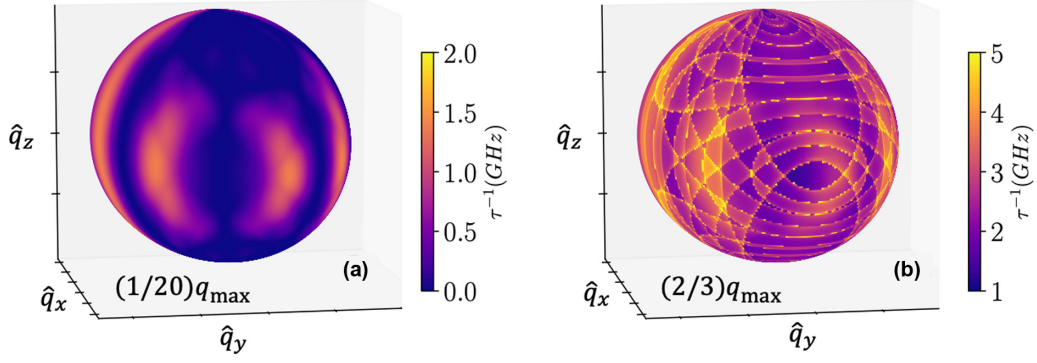


FIG. 5. Three-dimensional polar plots of the scattering rate $\tau^{-1}(\mathbf{q})$ (in GHz) versus incident angle (θ_i, ϕ_i) of an incoming phonon, holding phonon frequency constant. The results shown correspond to a twist boundary with $\theta = 5^\circ$ at the (a) long-wavelength limit [$q = q_{\max}/20$], where acoustic mismatch scattering dominates, and the (b) short-wavelength limit [$q = (2/3)q_{\max}$], where the periodic strain field scattering effect is picked up.

This cancellation can be seen in the long-wavelength limit of the Fourier-transformed strain fields, as Q_y approaches zero in the YZ array and Q_z approaches zero in the ZY array. The components $\tilde{\epsilon}_{13}$, $\tilde{\epsilon}_{12}$, and the sum of the two $\tilde{\epsilon}_{23}$ parts all vanish. The cancellation is additionally apparent in the $|x| \rightarrow \infty$ limit of the real-space analytic solutions for the strain at infinite screw dislocation arrays, as shown in Appendix C [27]. We can manually enforce this by omitting the $n' = 0$ term in the calculation of \tilde{V}_{YZ} or \tilde{V}_{ZY} [Eq. (8)] and instead treating the corresponding scattering term in the long-wavelength limit with the acoustic mismatch term \tilde{V}_{AM} as shown in Eq. (14).

B. Twist boundary results and discussion

The results discussed here describe Si-Si symmetric twist boundaries with various twist angles θ , and were calculated using the Si parameters in Table VI.

As previously noted in the case of the tilt boundary, the twist boundary exhibits a crossover in the frequency dependence of the relaxation time (τ) [23]. Long-wavelength phonons view the boundary as a planar defect defined by the rotational deformation, leading to the expected frequency-independent scattering. The relaxation time at this long-wavelength, or low-frequency, limit is plotted versus grain boundary angle in Fig. 6(c) and is seen to vary periodically with angle θ . This periodic relationship has been predicted previously and is a result of the symmetry of the Si acoustic properties [43]. Short-wavelength phonons, however, interact with the underlying periodic strain from the dislocation grid and pick up a phonon frequency dependence approaching $\tau \propto \omega^{-1}$ [Fig. 6(b)]. As a result, the overall thermal boundary resistance increases linearly with grain boundary angle because of the increasing strain scattering effects.

TABLE I. Twist boundary Fourier strain field components.

YZ array	ZY array
$\tilde{\epsilon}_{13} = \frac{ibQ_y}{2(Q_x^2 + Q_z^2)}$	$\tilde{\epsilon}_{12} = -\frac{ibQ_z}{2(Q_x^2 + Q_z^2)}$
$\tilde{\epsilon}_{23} = -\frac{ibQ_x}{2(Q_x^2 + Q_z^2)}$	$\tilde{\epsilon}_{23} = \frac{ibQ_x}{2(Q_x^2 + Q_z^2)}$

We can also compare these results to the symmetric tilt boundary scattering case (Fig. 7). In both grain boundary types, the rotational scattering is calculated from Eq. (14) using the grain boundary angle θ to determine the phonon velocity change at the interface. It should be kept in mind, however, that in the tilt case, the rotation is perpendicular to the plane of the interface. The spectral τ in both cases is approximately equal at the long-wavelength limit as a result of the cubic symmetry of the Si stiffness matrix and acoustic velocities (Fig. 11). However, for the twist boundary, the relaxation time decreases more rapidly with frequency in the dislocation scattering regime [Fig. 7(a)]. In the work of van der Merwe [36], a linear elasticity model for interfacial stresses and energies is applied to a generic material with cubic or tetragonal symmetry, and shows that for the same misorientation angle θ , twist boundaries exhibit slightly higher strain energy than tilt boundaries. The higher strain energy of the twist boundary can explain the reduced relaxation times at high phonon frequency, which leads to about 1.3 times the thermal boundary resistance of the tilt boundary [Fig. 7(b)].

The R_K from the Si-Si twist boundary model [Eq. (5)] is close to, although consistently lower than, previously reported molecular dynamics simulation results (see Table II). We also compare model predictions against R_K measurements of Si-Si twist boundaries using the 3ω method, an AC technique suited for thermal conductivity measurements of films, reported by Xu *et al.* [20]. In both cases, the magnitude of the thermal resistance depends on twist angle, and the R_K ratio between the 6.9° and 3.4° twist boundaries is similar. However, the measured thermal resistance is more than an order of magnitude larger than the model predictions. The model assumes a clean interface, while the interface in the physical material serves as a sink for additional defects and may contain roughness or oxidation effects [46,47]. In this particular experiment, a Si thin film was bonded to a Si substrate at varying twist angles. TEM images revealed a nanometer-thick disordered region at the boundary, which contributes additional thermal resistance [20,48,49]. A detailed modeling of these contributions is necessary to understand the experimental results.

A benefit of our approach is the ability to differentiate between the scattering contributions of the rotational defor-

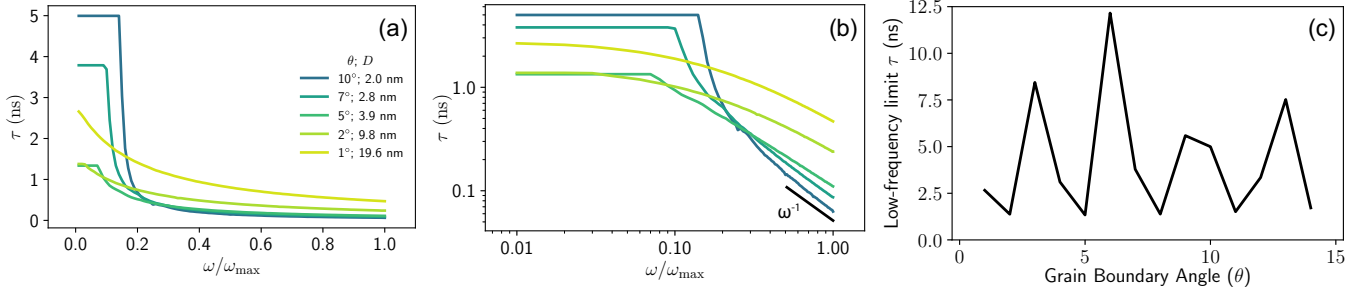


FIG. 6. Si-Si twist boundary scattering relaxation times. (a) Spectral phonon relaxation times for a Si-Si twist interface at various grain boundary angles. (b) The log-log plot of this relaxation time shows a power-law crossover from ω independent to $\sim\omega^{-1}$. (c) The long-wavelength limit of the relaxation time is plotted against grain boundary angle, revealing a periodic variation.

mation and the dislocation strain. The percentage contribution of the acoustic mismatch effect to R_K is only about 4–5% for most symmetric twist boundaries, and dislocation strain accounts for the rest of the scattering. This breakdown illustrates the significant role of the interfacial dislocation structure in the thermal resistance.

Finally, experimental investigations of twist boundary R_K show a correlation with the Read-Shockley grain boundary energy [50], which captures the strain energy produced by the dislocation structure at the grain boundary [20,21]. This observation corroborates the idea that dislocation strain is essential to understand the origins of interfacial thermal resistance. The Read-Shockley grain boundary energy is given by

$$E = \frac{Gb}{4\pi(1-\nu)}\theta(A - \ln(\theta)), \quad (16)$$

with dependencies on the misorientation angle θ , Burgers vector b , bulk modulus G , and Poisson ratio ν . The A factor captures the ratio between the dislocation core energy and strain energy contributions at the grain boundary. We set A equal to 0.23, following the previous work of Tai *et al.* [21], for the simple purposes of demonstrating the correlation with R_K . As shown in Fig. 8, R_K from the twist boundary model closely trends with the Read-Shockley strain energy, as expected.

IV. SEMICOHERENT HETEROINTERFACE SCATTERING

In this section, we apply the formalism of Sec. II to a semicoherent heterointerface.

A. Misfit dislocation strain and acoustic mismatch

Maintaining the geometry of Sec. II A, the semicoherent heterointerface is defined in the yz plane with two interpenetrating arrays of dislocations with misfit edge character [51]. As in the previous case of the tilt boundary [23], the deformation tensor is broken down into dilatational strain (ϵ_Δ), shear strain (ϵ_S), and rotation (ϵ_R), which act as independent scattering sources. These strain fields are related to those of the tilt boundary by a simple rotation, which places the extra half plane along the x axis, perpendicular to the boundary. They are given in real space in Appendix D. Table III lists the Fourier strain components for a single misfit edge dislocation in both the YZ and ZY arrays.

Figure 2 shows a normal component of the strain field from a single misfit dislocation array, and the cross section reveals a step function change in the dilatation at the interface (see pp. 695–697 of Ref. [27]). In fact, setting $Q_y = 0$ in the YZ array or $Q_z = 0$ in the ZY array yields $\tilde{\epsilon}_\Delta \propto i/Q_x$, which is precisely the Fourier transform of the Heaviside step function. As explained in Sec. I, this long-range dilatational strain effect is artificial, since the reference lattice parameter differs on either side of the interface. Therefore, the dilatational strain

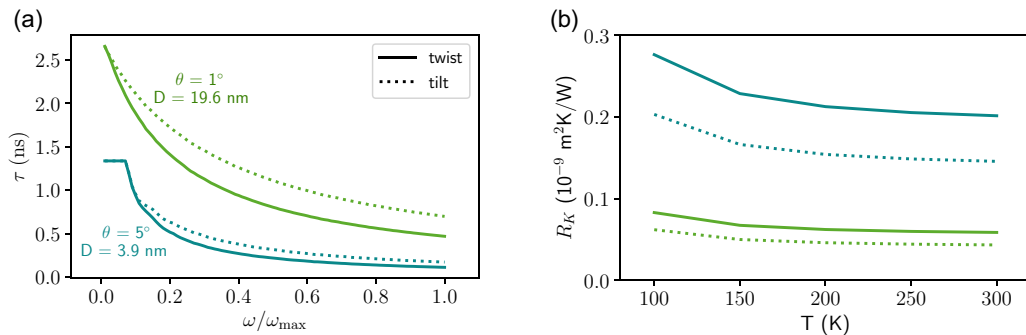


FIG. 7. The comparison of twist and tilt boundaries show that (a) the spectral relaxation time (τ) converges at the long-wavelength limit, but decreases faster in the frequency-dependent regime for the twist boundary. (b) The twist boundary, therefore, is predicted to have about 1.3 times the thermal boundary resistance (R_K).

TABLE II. Thermal boundary resistance (R_K in $\text{m}^2 \text{K}/\text{GW}$) comparison to previous theoretical and experimental literature results for the Si-Si symmetric twist boundary.

T (K)	Angle θ	R_K , literature MD [8,11,45]	R_K , this study Born-von Kármán
500	11.42°	0.61, 0.76, 1.1 Experimental [20]	0.30
300	6.9°	9.0	0.21
300	3.4°	6.7	0.13
300	$R_K(6.9^\circ)$ $R_K(3.4^\circ)$	1.3	1.6

at the long-wavelength limit is subtracted and treated via the acoustic impedance mismatch term described by Eq. (14).

Recently, Varnavides *et al.* introduced the strain mismatch model (SMM) [7], providing an *ab initio* framework for inelastic phonon scattering due to an interfacial strain perturbation. The SMM method is applied to treat a similar physical system, studying the dilatational strain scattering from a misfit dislocation array. By following the treatment of Carruthers (Eq. 4.91 of Ref. [38]), the derived scattering rate is found to be independent of the dislocation spacing and, as far as we can interpret, neglects the periodic strain fields local to the interface, which we find to be important in this work. Both previous works [7,38] additionally treat the step change in dilatation at a misfit dislocation array as a source of anharmonic strain scattering, which differs from the acoustic mismatch approach taken here.

B. Heterointerface results and discussion

The calculations below are performed for a Si-Ge interface using the parameters found in the Table VI. As in the tilt and twist boundary examples, the heterointerface relaxation time crosses over between planar-defect and linear-defect scattering. However, as expected due to the larger acoustic mismatch, the thermal resistance is significantly larger than in the twist boundary case. The acoustic mismatch effect alone, however, contributes only about 50% of the full thermal boundary resistance (see Fig. 9) predicted by the model, indicating a significant contribution of misfit dislocation strain scattering to the thermal resistance.

Table IV shows the thermal boundary resistance (R_K) results of our method assuming a Born-von Kármán (BvK) model for the phonon dispersion. The results show good agreement with previous calculations on Si-Ge heterojunctions using the DMM and MD simulations [4]. In the diffuse mismatch model, the overlap in the phonon density of states

TABLE III. Heterointerface Fourier strain field components.

YZ array	ZY array
$\tilde{\epsilon}_\Delta = \frac{ib(1-2\nu)}{(1-\nu)} \frac{Q_x}{(Q_x^2+Q_y^2)}$	$\tilde{\epsilon}_\Delta = \frac{ib(1-2\nu)}{(1-\nu)} \frac{Q_x}{(Q_x^2+Q_z^2)}$
$\tilde{\epsilon}_S = \frac{-ib}{(1-\nu)} \frac{Q_x Q_y^2}{(Q_x^2+Q_y^2)^2}$	$\tilde{\epsilon}_S = \frac{-ib}{(1-\nu)} \frac{Q_x Q_z^2}{(Q_x^2+Q_z^2)^2}$
$\tilde{\epsilon}_R = \frac{-2ibQ_y}{(Q_x^2+Q_y^2)}$	$\tilde{\epsilon}_R = \frac{-2ibQ_z}{(Q_x^2+Q_z^2)}$

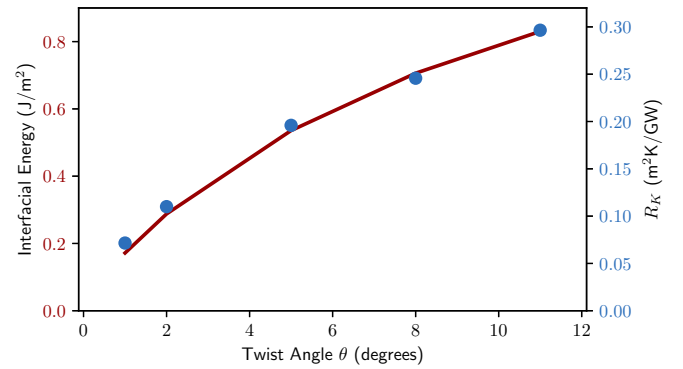


FIG. 8. Thermal boundary resistance (R_K) correlates with Read-Shockley grain boundary energy, as observed experimentally.

on either side of the interface determines the transmission probability. In contrast, the molecular dynamics simulation uses no model or assumption about the phonon scattering mechanism. We compare to the results from the largest simulation cell trialed in each of the previous MD studies [30,52]. Our results are also in line with the atomistic Green's function (AGF) approach, which circumvents the lattice dynamical matrix equation, and instead studies the impulse response of the system [53]. The AGF work additionally studied the influence of alloying at the interface and observed that R_K doubles with an alloy layer of just 1 nm. Finally, in the SMM [7], phonon transmission coefficients are evaluated through an iterative solution of the phonon Boltzmann transport equation to predict R_K . The SMM predicts a larger R_K , likely due to the first-principles anharmonicity treatment and differences in the treatment of the dilatation at the interface (see Sec. IV A).

The thermal boundary resistance R_K of the Si-Ge interface has also been investigated experimentally. The through-film thermal conductivity of superlattice films can be converted to a value for R_K by assuming that bulk phonon scattering is negligible [7], and the results for the largest reported period L (i.e., thickness of interlayers) are summarized in Table IV. While the R_K calculated here is comparable to the superlattice measurements, it is important to note that its value is affected by the coherent phonon dynamics present in superlattices. Additionally, Wang *et al.* [56] measured the R_K of a Si film bonded to a Ge substrate using the 3ω method, and reported an order-of-magnitude larger thermal boundary resistance. In their study, however, a ~ 3 -nm alloy layer is shown to form with additional interdiffusion persisting for ~ 10 nm around the interface, and this alloying effect predominates the interfacial thermal resistance. Interface quality can therefore have order-of-magnitude effects on the thermal transport [57].

V. CONCLUSION

In this study, we have focused on the thermal resistance of special low-energy interfaces, which can be decomposed into periodic arrays of dislocations. Specifically, we provide a formalism for the scattering effects of two orthogonal dislocation arrays combining to form a cross grid, and apply this model to describe symmetric twist boundaries and semicoherent heterointerfaces. Because our model explicitly incorporates information about the dislocation structure, we can capture

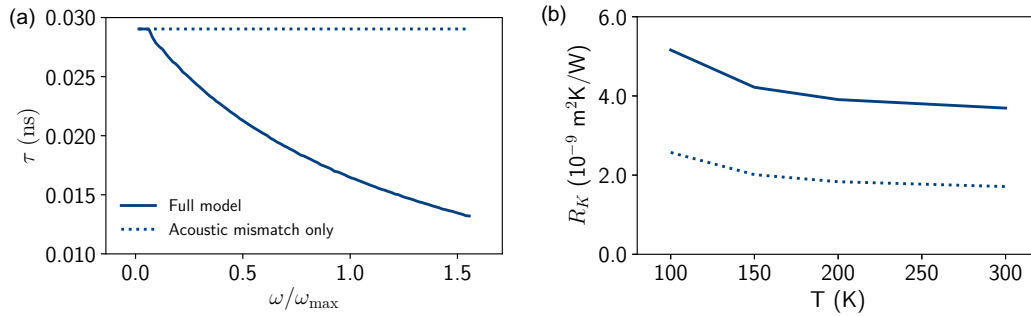


FIG. 9. Si-Ge heterointerface scattering using a Born–von Kármán phonon dispersion. (a) Spectral relaxation time for a Si-Ge heterointerface with a misfit dislocation spacing of 7 nm, comparing model with acoustic mismatch and dislocation strain (solid line) to the acoustic mismatch effect alone (dotted line). (b) Thermal boundary resistance predictions versus temperature from the heterointerface model with (solid line) and without (dotted line) dislocation strain scattering.

the effects of dislocation spacing and strain energy on scattering rates and transport coefficients. Additionally, whereas standard models of boundary scattering yield ω -independent, planar defect scattering, this model explicitly shows the onset of ω -dependent scattering stemming from the interactions of mid- to high-frequency phonons with interfacial dislocations. Finally, we address long-range deformations at the interface with an acoustic mismatch scattering treatment, within our perturbation theory framework. The transport predictions from this model agree well with results from molecular dynamics, but generally underestimate experimentally measured thermal resistances. However, this discrepancy may demonstrate the influence interfacial roughness and defect decoration can have on thermal resistance. The discussion presented here on interfacial thermal resistance, with comparisons of grain boundary type, angle, and energy, can accelerate an ICME microstructure engineering framework for thermal materials.

All scripts used to implement this boundary scattering model are available [58].

ACKNOWLEDGMENTS

This work was performed under the financial assistance award 70NANB19H005 from the U.S. Department of Commerce, National Institute of Standards and Technology, as part of the Center for Hierarchical Materials Design (CHiMaD).

S.G. and R.H. acknowledge support from the Office of Naval Research under a MURI program (Grant No. N00014-18-1-2429) and Air Force Office of Scientific Research under a MURI program (Grant No. FA9550-18-1-0479).

APPENDIX A: SCATTERING RATE CALCULATION

This Appendix outlines the main steps to arrive at the final working formula [Eq. (A7)] for the scattering rate Γ due to a dislocation grid. As before, the YZ array is composed of dislocation lines oriented along the z direction that are periodically spaced by D along the y direction. Conversely, the ZY array has dislocation lines oriented along the y direction that are periodically spaced by D along the z direction. Finally, the linear density of planar defects in the sample is given by $n_D = 1/L_x$. For ease of this discussion, we will start with an alternative representation of Fermi's golden rule, which relates Γ to the number density of defects (n_b), squared matrix element ($|M|^2$), and a phase-space factor (g) capturing all the final phonon states \mathbf{q}' that the incident phonon could scatter into:

$$\Gamma(\mathbf{q}) = n_b |M|^2 g(\omega_{\mathbf{q}}). \quad (\text{A1})$$

Here, n_b is the linear density of boundaries in the material and is approximately equal to $1/L$, where L is the average grain size in the material. As shown in Sec. II A, the scattering rate

TABLE IV. Room-temperature thermal boundary resistance (R_K in $\text{m}^2 \text{ K/GW}$) with comparison to theoretical and experimental literature results for Si-Ge heterointerface.

This work	Computational or theoretical				
	Ref. [30]		Ref. [52]	Ref. [7]	Ref. [53]
BvK	MD	DMM	MD	DMM	AGF
3.75	2.83	2.40	3.00	3.71	3.36
	Experimental (3ω method)				
Ref. [20]	Ref. [54]		Ref. [55]		
Bonded Films	Superlattice ($L = 14$ nm)	Superlattice ($L = 15$ nm)	Superlattice ($L = 27.5$ nm)		
31.4	2.14	3.62	6.28		

from the YZ and ZY dislocation grid can be computed separately. Therefore, here we will focus on deriving the scattering rate from the YZ array (Γ_{YZ}), and the Γ_{ZY} term can be written by analogy by enforcing periodicity along the z direction.

Starting with Eq. (7) (reproduced below), the Fourier transform of the periodic scattering potential for the YZ array is

$$\begin{aligned}\tilde{V}_{YZ} &= \iint dx dy \sum_{n=-\infty}^{\infty} V_1(x, y - nD) e^{-i(Q_x x + Q_y y)} \\ &= \sum_{n=-\infty}^{\infty} e^{-iQ_y nD} \tilde{V}_1(Q_x, Q_y).\end{aligned}\quad (\text{A2})$$

Here, V_1 is the real-space strain field around a single dislocation defect. We apply the Poisson summation formula to explicitly show the Dirac comb:

$$\sum_{n=-\infty}^{\infty} e^{-iQ_y nD} = \frac{2\pi}{D} \sum_{n'=-\infty}^{\infty} \delta(Q_y - Q_{n'}), \quad \left(Q_{n'} = \frac{2\pi n'}{D}\right).\quad (\text{A3})$$

$$\Gamma_{YZ}(\mathbf{q}) = \frac{n_D}{\hbar^2 v_g D^2} \sum_{n'=-\infty}^{\infty} \sum_{\sigma=\pm} \frac{(q_x^2 \mp q_x (q_x^2 + 2q_y Q_{n'} - Q_{n'}^2)^{1/2} + q_y Q_{n'})}{q(q_x^2 + 2q_y Q_{n'} - Q_{n'}^2)^{1/2}} |\tilde{V}_1(Q_x, n'\sigma, Q_{n'})|^2.\quad (\text{A7})$$

This is the working formula that we use for numerical calculation of scattering rate due to the YZ array of dislocations, and equivalently for the ZY array by switching the y and the z components.

Finally, to get the spectral relaxation time, we must average over the incident phonon wave-vector direction \hat{q} . We compute $\tau(\omega)$ as the weighted orientational average of the inverse scattering rate,

$$\tau(\omega) = \frac{\iint \Gamma^{-1} q_x^2 d\Omega}{\iint q_x^2 d\Omega} = \frac{3}{4\pi} \iint \Gamma^{-1} \frac{q_x^2}{q^2} d\Omega,\quad (\text{A8})$$

where $d\Omega$ is the element of solid angle for \hat{q} .

The spectral relaxation time can then be used to compute transport properties such as the lattice thermal conductivity in the phonon gas model,

$$\kappa_L = \frac{1}{3} \int C_s(\omega) v_g^2 \tau(\omega) d\omega,\quad (\text{A9})$$

using the expression

$$C_s(\omega) = \frac{3\hbar^2}{2\pi^2 k_B T^2} \frac{\omega^4 e^{\hbar\omega/k_B T}}{v_g v_p}\quad (\text{A10})$$

for the spectral heat capacity $C_s(\omega)$.

APPENDIX B: RELATING LANDAUER AND INTERFACIAL SCATTERING THEORY

There are several ways to model thermal transport in systems containing interfaces. Two common approaches are the Landauer formalism, which defines a phonon transmissivity and thermal boundary resistance, and scattering theory, which

Hence, \tilde{V}_{YZ} can be written as

$$\tilde{V}_{YZ} = \frac{2\pi}{D} \sum_{n'=-\infty}^{\infty} \delta(Q_y - Q_{n'}) \tilde{V}_1(Q_x, Q_y)\quad (\text{A4})$$

$$= \frac{2\pi}{D} \sum_{n'=-\infty}^{\infty} \delta(Q_y - Q_{n'}) \tilde{V}_1(Q_x, Q_{n'}).\quad (\text{A5})$$

We then square this result and integrate over all values \mathbf{q}' when computing the squared matrix element. Invoking Fermi's golden rule [Eq. (1)], the scattering rate for a phonon state \mathbf{q} is then

$$\begin{aligned}\Gamma_{YZ}(\mathbf{q}) &= \frac{n_b}{\hbar^2 D^2} \sum_{\tilde{n}=-\infty}^{\infty} \iiint d^3 \mathbf{q}' \delta(Q_z) \delta(\omega_{\mathbf{q}} - \omega_{\mathbf{q}'}) \\ &\quad \times |\tilde{V}_{YZ}(Q_x, Q_{n'})|^2 (1 - \hat{\mathbf{q}} \cdot \hat{\mathbf{q}}').\end{aligned}\quad (\text{A6})$$

This is the same as Eq. S41 of Ref. [23]. The phase-space term is implicitly enforced by the momentum and energy conservation laws imposed by the δ functions. These conservation rules restrict this integral to a discrete set of available \mathbf{q}' states. Equations S42–S48 of Ref. [23] reexpress these δ functions explicitly in terms of \mathbf{q}' to arrive at the final expression for Γ :

models the interfacial thermal resistance via an additional relaxation time that modifies the thermal conductivity of the total system (bulk material plus interfaces). Figure 10(a) depicts the temperature profiles implied by the Landauer theory (blue line) versus scattering theory (red line) approaches. If the mean free path of a phonon is equal to or longer than L_x , the homogeneously sloped red line better represents reality. If the mean free path is much shorter than L_x , the distance between interfaces, inhomogeneities in the temperature gradient are expected near interfaces, and the blue line may be more appropriate. It is important to keep in mind that materials tend to have a wide distribution of mean free paths, so the red line may better describe low-frequency phonons, while the blue line may better describe high-frequency phonons. Regardless, we can mathematically relate these two frameworks and define a relationship between the relaxation time and transmissivity.

The spectral thermal conductivity of the bulk, interface-free system is given by

$$\kappa_{\text{bulk}}(\omega) = \frac{1}{3} C_s(\omega) v_g(\omega)^2 \tau_{\text{bulk}}(\omega),\quad (\text{B1})$$

where τ_{bulk} describes scattering in the bulk material and may contain phonon-phonon and phonon-point defect scattering, for example. The thermal resistance due to a slab of this bulk material of length L_x is $(L_x \kappa_{\text{bulk}})^{-1}$.

1. Landauer theory

Within the Landauer approach, we define a spectral thermal boundary conductance h_B based on the transmissivity from side 1 to side 2 of the interface α_{12} and the reverse direction

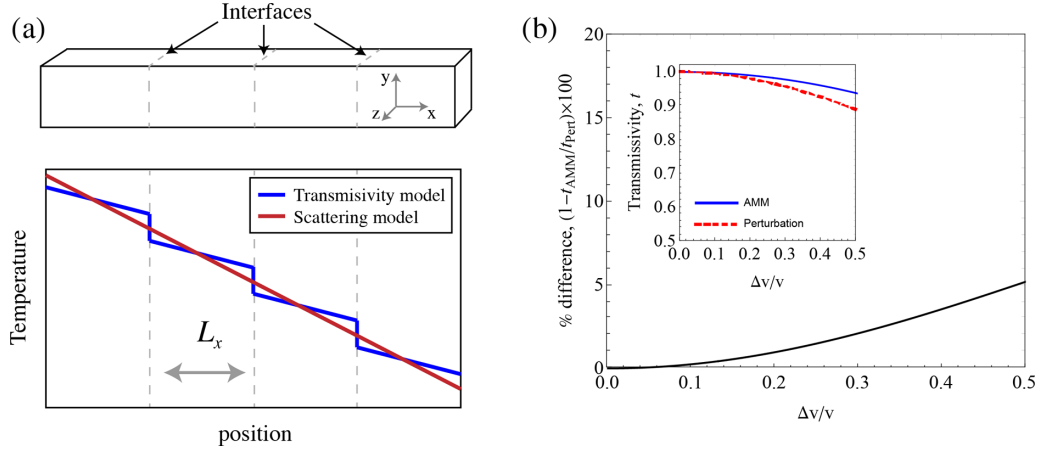


FIG. 10. (a) A schematic illustration of two common models used to describe heat conduction in materials with interfaces. The blue line depicts the Landauer-based model where a thermal boundary resistance arising from the conduction channel having an interfacial transmission probability or $t(\omega) > 0$ induces a sharply localized drop in temperature. The red line depicts a model based on phonon scattering theory and Matthiessen's rule, where each scattering mechanism contributes a scattering rate ($\tau(\omega)^{-1}$), and together they modify the material's thermal conductivity homogeneously. (b) A comparison between the transmissivity calculated using classical acoustic mismatch (AMM) theory and quantum perturbation theory. The two cases differ by no more than 5% up to $\Delta v/v = 0.5$.

α_{21} as

$$h_B(\omega) = \frac{1}{4} C_s(\omega) v_g(\omega) \left(\frac{\alpha_{12}(\omega)}{1 - \bar{\alpha}(\omega)} \right), \quad (\text{B2})$$

where $\bar{\alpha}(\omega) = (\alpha_{12}(\omega) + \alpha_{21}(\omega))/2$. The thermal boundary resistance of the interface is then defined by

$$1/R_K = h_B = \int_0^{\omega_m} h_B(\omega) d\omega. \quad (\text{B3})$$

Since the bulk material and interfaces are in series in this model, the total spectral thermal resistance is given by the sum of the bulk and interface resistances:

$$(L_x \kappa_L(\omega))^{-1} = (L_x \kappa_{\text{bulk}}(\omega))^{-1} + (h_B(\omega))^{-1}. \quad (\text{B4})$$

2. Interfacial scattering

The second interfacial resistance method treats the interface as an additional scattering mechanism, which can reduce the total phonon lifetime. The total thermal resistance of the same length of material, L_x , is given by Matthiessen's rule as the sum of the resistance due to bulk phonon scattering and the resistance due to boundary scattering,

$$(L_x \kappa_L(\omega))^{-1} = (L_x \kappa_{\text{bulk}}(\omega))^{-1} + (L_x \kappa_B(\omega))^{-1}. \quad (\text{B5})$$

In this work, we refer to the interface relaxation time as τ_B , giving

$$\kappa_B = \frac{1}{3} C_s(\omega) v_g(\omega)^2 \tau_B(\omega). \quad (\text{B6})$$

We can rewrite Eqs. (B5) and (B6) as

$$\kappa_L(\omega) = \frac{1}{3} C_s(\omega) v_g(\omega)^2 \tau_{\text{tot}}(\omega), \quad (\text{B7})$$

with $\tau_{\text{tot}}(\omega)$ given by the sum of scattering rates due to bulk processes such as phonon-phonon scattering (τ_{ph}) and interface scattering (τ_B):

$$\tau_{\text{tot}}(\omega)^{-1} = \tau_{\text{ph}}(\omega)^{-1} + \tau_B(\omega)^{-1}. \quad (\text{B8})$$

By equating Eqs. (B4) and (B5), we get $L_x \kappa_B(\omega) = h_B$. Now, when the relation $\tau_{12} = \tau_{21}(v_{g,1}/v_{g,2})$ is obeyed—which we will prove to hold true for our acoustic mismatch scattering potential next—we obtain Eq. (4). Here, the subscript 12 explicitly indicates that the phonon is approaching the interface from material 1, and vice versa for 21. This notation is omitted in the main text.

We now aim to directly compare the treatment of acoustic mismatch via our perturbation theory approach and the classical AMM treatment. To do so, we define an interface between two Debye solids where $v_1 = v + \Delta v/2$, $v_2 = v - \Delta v/2$, and density is unchanged, $\rho_1 = \rho_2$. Following the procedure presented by Hanus, Garg, and Snyder [23], and calculating the relaxation time due to the scattering potential given in Eq. (13), we find

$$\tau_{12}(\mathbf{q})^{-1} = \frac{\Delta v^2}{2L_x v_1 |\sin \theta \cos \phi|}. \quad (\text{B9})$$

At the acoustic mismatch limit, the planar defect produces a specular reflection, which scatters back into the density of states of side 1. The factor of v_g in the denominator, which comes from the density-of-states contribution, is therefore equal to v_1 . The spectral relaxation time can be obtained by using Eqs. (B9) and (A8):

$$\tau_{12}(\omega) = \frac{3}{2} L_x v_1 \Delta v^2. \quad (\text{B10})$$

Note that the relation $\tau_{12} = \tau_{21}(v_2/v_1)$ holds, since the factor of v_1 is associated with the density of states into which the phonon is scattering (i.e., reflection back into material 1). The details regarding the matrix element contribution to τ result in no change to the final result when inverting the problem from 12 to 21.

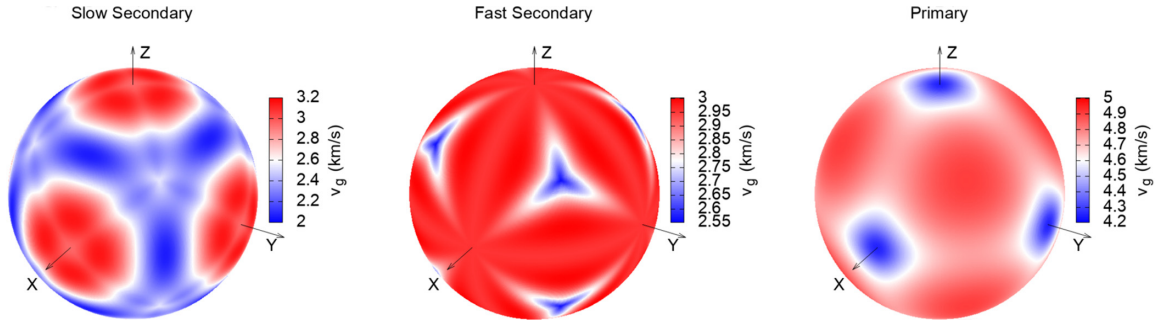


FIG. 11. Group velocity slowness plots for silicon: direction dependence of the acoustic phonon group velocities plotted on a unit sphere. Fast secondary and slow secondary correspond approximately to the two transverse branches, and primary is approximately the longitudinal branch. Produced using the CHRISTOFFEL package [42].

Using Eq. (B10) with Eq. (4), we obtain for the perturbation theory transmissivity

$$t_{\text{Pert}} = \frac{1}{\frac{1}{2}\left(\frac{\Delta v}{v}\right)^2 + 1}. \quad (\text{B11})$$

In the classical AMM theory, the transmissivity is given by [4]

$$t_{\text{AMM}} = \frac{4Z_1Z_2}{(Z_1 + Z_2)^2}, \quad (\text{B12})$$

where $Z_i = \rho_i v_{s,i}$ is the acoustic impedance of side i , and ρ_i is its mass density. The two cases are directly compared in Fig. 10(b) and they differ by no more than 5% up to $|\Delta v/v| = 0.5$.

APPENDIX C: TWIST BOUNDARY STRAIN FIELD DETAILS

The displacement vector field for a screw dislocation has only one nonzero component oriented along the line of the dislocation. Therefore, a dislocation with Burgers vector (b) parallel to \hat{z} has the following displacement field (see p. 60 of Ref. [41]):

$$\begin{aligned} \mathbf{u}_n &= (0, 0, u_z), \\ u_{3,n} &= \frac{b}{2\pi} \arctan\left(\frac{y}{x}\right). \end{aligned} \quad (\text{C1})$$

The displacement produces a pure shear state, with only two nonzero strain components:

$$\begin{aligned} \epsilon_{xz} = \epsilon_{zx} &= \frac{1}{2} \frac{\partial u_z}{\partial x} = -\frac{by}{4\pi(x^2 + y^2)}, \\ \epsilon_{yz} = \epsilon_{zy} &= \frac{1}{2} \frac{\partial u_z}{\partial y} = \frac{bx}{4\pi(x^2 + y^2)}. \end{aligned} \quad (\text{C2})$$

Next, we will consider the YZ array of screw dislocations spaced by D along the y axis in order to model a low-angle twist boundary. The stress components from the dislocation array $\epsilon_{ij}^{\text{YZ}}$ can be determined from the following summation:

$$\epsilon_{ij}^{\text{YZ}} = \sum_{n=-\infty}^{\infty} \epsilon_{ij}(x, y - nD). \quad (\text{C3})$$

Analytic solutions to the above summation can be obtained, and are shown below (see pp. 698–700 of Ref. [27]):

$$\begin{aligned} \epsilon_{xz}^{\text{YZ}} &= -\frac{b}{2D} \left(\frac{\sin(2\pi y/D)}{\cosh(2\pi x/D) - \cos(2\pi y/D)} \right), \\ \epsilon_{yz}^{\text{YZ}} &= \frac{b}{2D} \left(\frac{\sinh(2\pi x/D)}{\cosh(2\pi x/D) - \cos(2\pi y/D)} \right). \end{aligned} \quad (\text{C4})$$

One can then evaluate the limit as $|x| \rightarrow \infty$:

$$\lim_{x \rightarrow \infty} \epsilon_{xz}^{\text{YZ}} = 0, \quad (\text{C5})$$

$$\lim_{x \rightarrow \infty} \epsilon_{yz}^{\text{YZ}} = \text{sgn}(x) \frac{b}{2D}.$$

The $\epsilon_{yz}^{\text{YZ}}$ shear strain component persists at the long-range limit, converging to a constant value. This is energetically prohibitive for the twist boundary as a whole and shows the importance of including the ZY array of dislocations with sense vector along the y axis, periodically spaced on the z axis. The strain components from this array are the negative of Eq. (C4) with y and z swapped, and their long-range limits are

$$\lim_{x \rightarrow \infty} \epsilon_{xz} = 0, \quad (\text{C6})$$

$$\lim_{x \rightarrow \infty} \epsilon_{yz} = -\text{sgn}(x) \frac{b}{2D}, \quad (\text{C7})$$

which exactly cancel the far-field strain of the first array if both share the same b/D ratio [27].

APPENDIX D: HETEROINTERFACE STRAIN FIELD DETAILS

As with the twist boundary, the heterointerface is taken to lie in the yz plane with two interpenetrating arrays of dislocations, but now with edge character. Therefore, the strain fields are essentially equivalent to the tilt boundary case, requiring only a rotation such that the extra half plane points in the x direction. The strain field components are listed in Table V for one dislocation through the origin in each of the two arrays. The notation follows Ref. [23].

Again, considering the YZ array, analytic solutions exist for the real-space sum over the misfit edge dislocations periodically spaced by D . The analytic solutions for the three

TABLE V. Heterointerface strain field components.

YZ array	ZY array
$\epsilon_{\Delta} = \frac{-b(1-2\nu)}{2\pi(1-\nu)} \frac{x}{(x^2+y^2)}$	$\epsilon_{\Delta} = \frac{-b(1-2\nu)}{2\pi(1-\nu)} \frac{x}{(x^2+z^2)}$
$\epsilon_S = \frac{b}{4\pi(1-\nu)} \frac{y(y^2-x^2)}{(x^2+y^2)^2}$	$\epsilon_S = \frac{b}{4\pi(1-\nu)} \frac{z(z^2-x^2)}{(x^2+z^2)^2}$
$\epsilon_R = \frac{b}{\pi} \frac{y}{x^2+y^2}$	$\epsilon_R = \frac{b}{\pi} \frac{z}{x^2+z^2}$

independent nonzero strain components ϵ_{ij}^{YZ} in a Cartesian basis are (see pp. 695–697 of Ref. [27]) [36]

$$\epsilon_{xx}^{YZ} = \frac{b}{4(1-\nu)D} \left[\frac{-2\nu S_X(C_X - c_Y) + 2\pi X(C_X c_Y - 1)}{(C_X - c_Y)^2} \right], \quad (D1)$$

$$\epsilon_{yy}^{YZ} = \frac{b}{4(1-\nu)D} \left[\frac{2(1-\nu)S_X(C_X - c_Y) - 2\pi X(C_X c_Y - 1)}{(C_X - c_Y)^2} \right], \quad (D2)$$

$$\epsilon_{xy}^{YZ} = \frac{b}{2(1-\nu)D} \left[s_Y \left(\frac{2\pi X S_X - C_X + c_Y}{(C_X - c_Y)^2} \right) \right], \quad (D3)$$

where $X \equiv x/D$, $Y \equiv y/D$, $s_Y \equiv \sin 2\pi Y$, $c_Y \equiv \cos 2\pi Y$, $S_X \equiv \sinh 2\pi X$, and $C_X \equiv \cosh 2\pi X$.

We can again evaluate the limit as $|x| \rightarrow \infty$:

$$\lim_{x \rightarrow \infty} \epsilon_{xx}^{YZ} = \text{sgn}(x) \frac{-b\nu}{2(1-\nu)D}, \quad (D4)$$

$$\lim_{x \rightarrow \infty} \epsilon_{yy}^{YZ} = \text{sgn}(x) \frac{b}{D}, \quad (D5)$$

$$\lim_{x \rightarrow \infty} \epsilon_{xz}^{YZ} = 0. \quad (D6)$$

Here, the dilatation strain components (ϵ_{xx}^{YZ} and ϵ_{yy}^{YZ}) persist in the far-field limit, while the shear strain decays. Additionally, the far-field dilatational strain is not canceled out by the ZY array. However, as noted in the text, the nonzero dilatation in the far field is artificial since the reference lattices are different on either side of the interface. We reiterate that this far-field dilatational strain is subtracted and treated with an acoustic mismatch term capturing the step-function change in stiffness matrix at the interface.

APPENDIX E: CHRISTOFFEL EQUATION

The Christoffel matrix C is obtained from the rank-4 stiffness tensor c_{ijkl} for a unit vector \hat{n} denoting the phonon direction of propagation as follows [42]:

$$C_{ij} = \sum_{jkl} n_j c_{ijkl} n_k. \quad (E1)$$

From this, one can then evaluate the following eigenvalue problem to arrive at the phase velocity v_p of an acoustic phonon traveling in the direction \hat{n} with polarization vector δ :

$$\sum_{ij} (C_{ij} - \delta_{ij} v_p^2) s_j = 0. \quad (E2)$$

By solving this equation for different \hat{n} , it is possible to generate a slowness surface, or diagram of the direction-dependent group (v_g) or phase velocity (v_p) of the acoustic phonons in a material. As discussed in Ref. [42], the acoustic v_g and v_p differ slightly in terms of direction alone, as described by the power flow angle Ψ , where $v_p = v_g \cos \Psi$. The group velocity direction indicates the direction in which energy travels, which can deviate from the wave-front propagation direction described by the phase velocity. Figure 11 shows the group velocity slowness plots of the three phonon polarizations for Si.

Both the twist boundary and semicoherent interface models require solving the Christoffel equations to calculate the magnitude change of phonon velocity at the boundary Δv for a fixed incident phonon direction. In the twist boundary, Δv comes solely from the misorientation or, equivalently, the rotation of the slowness plots at the boundary. In contrast, in the Si-Ge heterointerface, for example, we calculate slowness plots for both the Si and Ge lattices, and compute Δv from the differences in acoustic velocity between the two materials for a fixed phonon direction. A misorientation could also be incorporated in the heterointerface by applying a relative rotation to the Ge slowness plot with respect to Si, for example.

APPENDIX F: MODEL PARAMETERS

The model parameters are summarized in Table VI with the values used for the Si-Si twist boundary and Si-Ge heterointerface examples discussed in the text. Across a temperature range of 100–800 °C, the temperature dependence of the input parameters due to lattice thermal expansion had a

TABLE VI. Parameters used in model.

Properties	Silicon	Germanium
Speed of sound, v_s (m/s) [59]	6084	5400
Atoms per unit cell, N	2	2
Volume per atom, V (Å ³) [59]	19.7	22.7
Density, ρ (kg/m ³)	2330	5323
Stiffness coefficients, c_{11} , c_{12} , c_{44} (GPa) [60,61]	165.6, 63.9, 79.5	126.0, 44.0, 67.7
Bulk modulus, G (GPa) [60]	97.83	
Grüneisen parameter, γ [23]	1	

negligible impact on the phonon relaxation time predictions. However, temperature-dependent inputs could be determined from quasiharmonic density functional theory calculations, for example.

The most computationally demanding portion of the model is the calculation of the spectral relaxation time, owing to the integrals over incident phonon direction and

phonon frequency. Running serially on a laptop, the calculation of each spectral relaxation time value $\tau(\omega)$ takes 2.16 min. We find that a spline of 50 spectral relaxation time $\tau(\omega)$ values are sufficient to converge the thermal boundary resistance R_K . Therefore, running serially on a laptop, each thermal boundary resistance calculation takes approximately 2 h.

-
- [1] M. G. Kanatzidis, *Chem. Mater.* **22**, 648 (2010).
- [2] R. Prasher, *Appl. Phys. Lett.* **94**, 041905 (2014).
- [3] A. Sood, R. Cheaito, T. Bai, H. Kwon, Y. Wang, C. Li, L. Yates, T. Bougher, S. Graham, M. Asheghi, M. Goorsky, and K. E. Goodson, *Nano Lett.* **18**, 3466 (2018).
- [4] E. T. Swartz and R. O. Pohl, *Rev. Mod. Phys.* **61**, 605 (1989).
- [5] J. Hickman and Y. Mishin, *Phys. Rev. Mater.* **4**, 033405 (2020).
- [6] R. S. Prasher and P. E. Phelan, *J. Heat Transfer* **123**, 105 (2001).
- [7] G. Varnavides, A. S. Jermyn, P. Anikeeva, and P. Narang, *Phys. Rev. B* **100**, 115402 (2019).
- [8] P. K. Schelling, S. R. Phillpot, and P. Keblinski, *J. Appl. Phys.* **95**, 6082 (2004).
- [9] Y. Zhang, D. Ma, Y. Zang, X. Wang, and N. Yang, *Front. Energy Res.* **6**, 1 (2018).
- [10] Q. Meng, L. Wu, and Y. Zhu, *Phys. Rev. B* **87**, 064102 (2013).
- [11] S.-H. Ju and X.-G. Liang, *J. Appl. Phys.* **113**, 053513 (2013).
- [12] D. G. Cahill, W. K. Ford, K. E. Goodson, G. D. Mahan, A. Majumdar, H. J. Maris, R. Merlin, and S. R. Phillpot, *J. Appl. Phys.* **93**, 793 (2003).
- [13] W. Xiong and G. B. Olson, *MRS Bull.* **40**, 1035 (2015).
- [14] J. P. Crocombette and L. Gelebart, *J. Appl. Phys.* **106**, 083520 (2009).
- [15] K. Gordiz and A. Henry, *Sci. Rep.* **6**, 23139 (2016).
- [16] A. Giri and P. E. Hopkins, *Sci. Rep.* **7**, 11011 (2017).
- [17] P. E. Hopkins, J. C. Duda, S. P. Clark, C. P. Hains, T. J. Rotter, L. M. Phinney, and G. Balakrishnan, *Appl. Phys. Lett.* **98**, 161913 (2011).
- [18] S. I. Kim, H. A. Mun, H. S. Kim, S. W. Hwang, J. W. Roh, D. J. Yang, W. H. Shin, X. S. Li, Y. H. Lee, G. J. Snyder, and S. W. Kim, *Science* **348**, 109 (2015).
- [19] H. S. Kim, S. D. Kang, Y. Tang, R. Hanus, and G. J. Snyder, *Mater. Horiz.* **3**, 234 (2016).
- [20] D. Xu, R. Hanus, Y. Xiao, S. Wang, G. J. Snyder, and Q. Hao, *Mater. Today Phys.* **6**, 53 (2018).
- [21] K. Tai, A. Lawrence, M. P. Harmer, and S. J. Dillon, *Appl. Phys. Lett.* **102**, 034101 (2013).
- [22] Y.-j. Kim, L.-d. Zhao, M. G. Kanatzidis, and D. N. Seidman, *Appl. Mater. Interfaces* **9**, 21791 (2017).
- [23] R. Hanus, A. Garg, and G. J. Snyder, *Commun. Phys.* **1**, 78 (2018).
- [24] C. Hua and A. J. Minnich, *Semicond. Sci. Technol.* **29**, 124004 (2014).
- [25] Z. Wang, J. E. Alaniz, W. Jang, J. E. Garay, and C. Dames, *Nano Lett.* **11**, 2206 (2011).
- [26] A. Anderson, in *Phonon Scattering in Condensed Matter*, Springer Series in Solid-State Sciences, Vol. 51 (Springer, Berlin, 1984).
- [27] W. Cai and W. Nix, in *Imperfections in Crystalline Solids* (Cambridge University Press, Cambridge, U.K., 2016), pp. 688–700.
- [28] D. Wolf, *Scr. Metall.* **23**, 1713 (1989).
- [29] C. Monachon, L. Weber, and C. Dames, *Annu. Rev. Mater. Res.* **46**, 433 (2016).
- [30] E. S. Landry and A. J. H. McGaughey, *Phys. Rev. B* **80**, 165304 (2009).
- [31] W. Zhang, T. S. Fisher, and N. Mingo, *J. Heat Transfer* **129**, 483 (2007).
- [32] C. Dames and G. Chen, *J. Appl. Phys.* **95**, 682 (2004).
- [33] G. Chen, *Phys. Rev. B* **57**, 14958 (1998).
- [34] Z. Chen, Z. Wei, Y. Chen, and C. Dames, *Phys. Rev. B* **87**, 125426 (2013).
- [35] G. Gottstein, *Grain Boundary Migration in Metals: Thermodynamics, Kinetics, Applications*, 2nd ed. (CRC Press, Boca Raton, FL, 2009).
- [36] J. H. van der Merwe, *Proc. Phys. Soc., Sect. A* **63**, 616 (1950).
- [37] P. Carruthers, *Phys. Rev.* **114**, 995 (1959).
- [38] P. Carruthers, *Rev. Mod. Phys.* **33**, 92 (1961).
- [39] M. Omini and A. Sparavigna, *Phys. Rev. B* **61**, 6677 (2000).
- [40] P. G. Klemens, *Proc. Phys. Soc., Sect. A* **68**, 1113 (1955).
- [41] J. P. Hirth and J. Lothe, *Theory of Dislocations*, 2nd ed. (Wiley, New York, 1982).
- [42] J. W. Jaeken and S. Cottenier, *Comput. Phys. Commun.* **207**, 445 (2016).
- [43] R. Brown, *J. Phys. C* **16**, 1009 (1983).
- [44] J. Carrete, B. Vermeersch, A. Katre, A. van Roekeghem, T. Wang, G. K. Madsen, and N. Mingo, *Comput. Phys. Commun.* **220**, 351 (2017).
- [45] J. K. Bohrer, K. Schröder, L. Brendel, and D. E. Wolf, *AIP Adv.* **7**, 045105 (2017).
- [46] Y. Yu, C. Zhou, S. Zhang, M. Zhu, M. Wuttig, C. Scheu, D. Raabe, G. J. Snyder, B. Gault, and O. Cojocaru-Mirédin, *Mater. Today* **32**, 260 (2020).
- [47] M. Khafizov, I. W. Park, A. Chernatynskiy, L. He, J. Lin, J. J. Moore, D. Swank, T. Lillo, S. R. Phillpot, A. El-Azab, and D. H. Hurley, *J. Am. Ceram. Soc.* **97**, 562 (2014).
- [48] H. S. Shin, S. G. Jeon, J. Yu, Y. S. Kim, H. M. Park, and J. Y. Song, *Nanoscale* **6**, 6158 (2014).
- [49] G. Li, J. He, Q. An, S. I. Morozov, S. Hao, P. Zhai, Q. Zhang, W. A. Goddard, and G. J. Snyder, *Acta Mater.* **169**, 9 (2019).
- [50] W. T. Read and W. Shockley, *Phys. Rev.* **78**, 275 (1950).
- [51] Y. Yao, T. Wang, and C. Wang, *Phys. Rev. B* **59**, 8232 (1999).

- [52] T. Zhan, S. Minamoto, Y. Xu, Y. Tanaka, and Y. Kagawa, *AIP Adv.* **5**, 047102 (2015).
- [53] X. Li and R. Yang, *Phys. Rev. B* **86**, 054305 (2012).
- [54] T. Borca-Tasciuc, W. Liu, J. Liu, T. Zeng, D. W. Song, C. D. Moore, G. Chen, K. L. Wang, M. S. Goorsky, T. Radetic, R. Gronsky, T. Koga, and M. S. Dresselhaus, *Superlattices Microstruct.* **28**, 199 (2000).
- [55] S.-M. Lee, D. G. Cahill, and R. Venkatasubramanian, *Appl. Phys. Lett.* **70**, 2957 (1997).
- [56] S. Wang, D. Xu, R. Gurunathan, G. J. Snyder, and Q. Hao, *J. Materiomics* **6**, 248 (2020).
- [57] P. E. Hopkins, *Int. Scholarly Res. Not. Mech. Eng.* **2013**, 682586 (2013).
- [58] <https://github.com/RamyaGuru/BoundaryScattering>.
- [59] E. S. Toberer, A. Zevalkink, and G. J. Snyder, *J. Mater. Chem.* **21**, 15843 (2011).
- [60] M. A. Hopcroft, W. D. Nix, and T. W. Kenny, *J. Microelectromech. Syst.* **19**, 229 (2010).
- [61] J. M. Escalante, *Comput. Mater. Sci.* **152**, 223 (2018).

Correction: The previously published order of authors was presented incorrectly and has been fixed, and the affiliations are now identified by superscript numbers.